Desalination and Water Treatment
www.deswater.com
doi: 10.5004/dwt.2020.25999

197 (2020) 157–169
September

Adsorption performance and response surface optimization of boron in desalinated seawater by UiO-66-NH_2

Yannan Jia[a,b,*], Jiacheng Li[c], Zijie Wang[c], Xiaomei Wu[a,b], Kai Xu[c], Zheng Wang[c]

[a]*State Key Laboratory of Simulation and Regulation of Water Cycle in River Basin, China Institute of Water Resources and Hydropower Research, Beijing 100038, China, Tel. +86 10 68786961; emails: jiayn@iwhr.com (Y. Jia), berry0603@126.com (X. Wu)*
[b]*China Institute of Water Resources and Hydropower Research, Beijing 100038, China*
[c]*School of Civil Engineering, Nanjing Forestry University, Longpan Road 159#, Nanjing 210037, China, emails: 15240166079@163.com (J. Li), wzj854333843@163.com (Z. Wang), horizonxk@163.com (K. Xu), wangzheng@njfu.edu.cn (Z, Wang)*

Received 23 October 2019; Accepted 16 April 2020

ABSTRACT

Metal-organic framework UiO-66-NH_2 was studied as an adsorbent for effective boron removal from desalination seawater for the first time. First, UiO-66-NH_2 was synthesized using the solvothermal method and then characterized in terms of N_2 adsorption/desorption isotherms, zeta potential, scanning electron microscopy, X-ray diffraction, Fourier-transform infrared spectroscopy, and thermogravimetric analysis. Based on the experimental design of response surface methodology, the adsorption of boron on UiO-66-NH_2 was optimized using three independent variables: adsorbent dosage (60–80 mg/L), pH (5–7), and temperature (298–318 K). Under the optimized conditions, the maximum adsorption capacity was predicted to reach 24.54 mg/g. Investigation of the kinetics and isotherms revealed that the pseudo-second-order kinetics model and the Langmuir isotherm can well cover the adsorption data of boron. Thermodynamic parameters showed that the adsorption of boron by UiO-66-NH_2 is spontaneous and feasible. UiO-66-NH_2 also exhibits good reproducibility. It is a highly practical sorbent that can be used to remove boron from desalination seawater.

Keywords: UiO-66-NH_2; Boron adsorption; Response surface optimization; Kinetics; Thermodynamics; Isotherms

1. Introduction

With the increasingly serious problem of water pollution, the shortage of water resources has become increasingly prominent [1]. Many countries have invested in the study of seawater desalination and the establishment of seawater desalination plants [2]. Boron usually exists in the form of boric acid in seawater at a concentration of approximately 5–6 mg/L [3]. Since boron above a certain concentration will have a negative impact on people and plants, the World Health Organization stipulates that the limit of boron concentration in drinking water is 2.4 mg/L [4]. In irrigation water, the maximum allowable boron concentration ranges from 0.3 to 1 mg/L, according to various national regulations [5,6]. Therefore, the concentration of boron after desalination affects the use of desalinated seawater to a certain extent. Common desalination methods have difficulty removing boron effectively because its amount in untreated seawater is small and uncharged [7]. Among many desalination techniques, reverse osmosis is the preferred method. A single-stage reverse osmosis membrane can reduce the boron concentration in an osmotic solution to approximately 0.9–1.8 mg/L [3,8]. This is not enough to reduce the concentration of boron to a safe level, however, making it necessary to further remove boron from desalinated seawater.

* Corresponding author.

At present, several methods have been developed to remove boron from water bodies, such as reverse osmosis, adsorption, electrocoagulation, ion exchange, and chemical coagulation [9–12]. Although these methods show a positive effect on boron removal, some drawbacks such as the high operating costs and limited absorption of boron at low concentrations limited their practical applications in the desalination of seawater. Among these techniques, adsorption is one of the most promising due to its low cost, good absorption of boron, and easy regeneration [10,13]. There have been many studies of different boron removal adsorbents, including natural minerals [14], chelating resins [15], and nanometer materials [16]. One of the most representative boron adsorbents is amberlite IRA-743, produced by the Rohm and Haas Company (United States). Its adsorption capacity is approximately 10 mg/g, and it is widely used in commercial applications [17]. This amount of boron adsorption capacity is not enough for desalinated seawater, however. In order to improve the efficiency of boron removal and reduce the cost, a new adsorbent with a greater adsorption capacity is urgently needed.

Metal-organic frameworks (MOFs) are porous materials with network structures, which can be formed by organic ligands and metal ions and create complex metal ligands by self-assembly [18]. MOFs materials have unique performance advantages, such as controllable pore size, modified pore surface, low density and high surface area. Therefore, this new type of porous material has been widely used in many fields, including gas purification, gas separation, gas storage, energy storage and photocatalysis [19–23]. In recent years, MOFs have been drawn more attention in water treatment due to their large specific surface area, adjustable channel, and ease of modification [24]. According to the existing research, it has shown good performance in many fields such as the treatment of antibiotics, dyes, heavy metal and radionuclides [25–29]. Among them, UiO-66-NH_2 has attracted widespread attention due to its strong heat resistance and chemical stability, various preparation methods, and ease of modification [30]. Currently, UiO-66-NH_2 has been investigated for the removal Pb(II) [30], Cr(VI) [31], and methylene blue [32] from water. UiO-66-NH_2 also has the potential to remove boron from desalinated seawater, although no related research has yet been reported.

The primary objective of this study was to evaluate the adsorption properties of boron on UiO-66-NH_2. This study analyzed the isothermal, kinetic, and thermodynamic characteristics of boron adsorption. The optimization of removal procedures, as well as the determination of the experimental variables (pH, adsorbent dosage, temperature) and their interactions, were investigated using response surface methodology.

2. Materials and methods

2.1. Materials

The primary chemicals utilized in this study were all pure and of analytical grade, and the experimental water was deionized. Zirconium tetrachloride ($ZrCl_4$) and 2-aminoterephthalic acid (H_2BDC-NH_2) were purchased from the Shanghai Aladdin Shenghua Technology Co., Ltd., (Shanghai, China). N,N-dimethylformamide (DMF), methanol, nitric acid (HNO_3), hydrochloric acid (HCl), and sodium hydroxide (NaOH) were purchased from the Nanjing Chemical Reagent Co., Ltd., (Nanjing, China).

2.2. Preparation of UiO-66-NH_2

UiO-66-NH_2 was solvothermal synthesized based on the method of Rui et al. [19]. Zirconium chloride ($ZrCl_4$, 0.772 g) and 2-aminoterephthalic acid (H_2BDC-NH_2, 0.556 g) were dissolved in DMF (80 mL). The mixture was then transferred to a 100 mL polytetrafluoroethylene-lined stainless steel autoclave and heated for 24 h at 393 K. The mixture was cooled to room temperature, and the yellow powder was obtained by centrifugation at 4,000 rpm. After washing 3 times with DMF and methanol, the powder was immersed in 80 mL of methanol solution and treated in a reactor at 373 K for 12 h. UiO-66-NH_2 was obtained by centrifuging the solution with methanol and drying it in a vacuum oven at 373 K for 12 h.

2.3. Characterization methods

The Brunauer–Emmett–Teller (BET) specific surface area, pore size distribution, and pore volume were examined using a fully automatic specific surface area and pore size distribution meter (Micromeritics, ASAP2020 HD88, USA). The sample was measured for the nitrogen adsorption/desorption isotherm at 77 K after degassing at 323 K for 24 h. The specific surface area was estimated using the BET equation. The pore size was estimated using the density functional theory (DFT) method. The high-resolution images of UiO-66-NH_2 after gold coating were captured using a field emission scanning electron microscope (JEOL, JSM-7600F, Japan). The accelerating voltage was 20 kV, and the images were taken at 10,000× magnification. The crystalline structure of UiO-66-NH_2 was determined by the X-ray diffraction (XRD) patterns on an X'Pert diffractometer (Rigaku, Ultima IV, Japan) with Cu-Ka radiation at a scanning speed of 0.02°/s and a temperature of 27°C, ranging from 5°C to 80°C. The chemical components of UiO-66-NH_2 were analyzed using Fourier-transform infrared spectroscopy (FTIR) (Thermo Scientific, Nicolet IS5, USA), by taking 32 scans from 400 to 4,000 cm^{-1} with a resolution of 2 cm^{-1} using the potassium bromide pellet technique. Thermogravimetric (TG) analysis was performed using a thermal analyzer (TA, Q500, USA). Experiments were carried out under an N_2 atmosphere (30 mL/min flow rate) at a heating rate of 10°C/min from room temperature to 800°C. The particle size and zeta potential of UiO-66-NH_2 were analyzed with a laser particle size analyzer (Malvern, ZS90, UK). The zeta potential determination procedure was as follows: 0.1 g of UiO-66-NH_2 was placed in 100 mL of pure water and shaken. The pH was adjusted to 4, 5, 6, 7, 8, 9, and 10 with HCl and NaOH. The prepared UiO-66-NH_2 suspension was allowed to stand for 5 min, and the zeta potential was then measured.

2.4. Adsorption experiments

Plastic equipment was used throughout the experiment in order to avoid the effects of boron on the glass

equipment. Boric acid was prepared as a stock solution in deionized water, and 50 mL of the desired concentration of boron was mixed with UiO-66-NH_2. Afterward, the pH was adjusted with 0.1 M NaOH and HNO_3 solution, and the mixture was spun at 160 rpm for a specified time. Next, the mixture was filtered using a 0.22 μm filter, and the supernatant was collected. The remaining boron concentration was determined using inductively coupled plasma mass spectrometry (PE, NeXion 300X, USA).

The effect of pH on the boron adsorption capacity of UiO-66-NH_2 was examined for a wide range of pH values (4, 5, 6, 7, 8, 9, and 10). In this experiment, the initial adsorbate concentration, adsorbent dose, contact time, and temperature were controlled at 2 mg/L, 60 mg/L, 420 min, and 27°C, respectively. The effect of adsorbent dose on the boron adsorption capacity of UiO-66-NH_2 was studied at adsorption doses of 40, 60, 80, 100, and 120 mg/L. In this experiment, the adsorbate concentration, temperature, contact time, and pH were controlled at 2 mg/L, 27°C, 420 min, and 6, respectively.

The adsorption capacity [Eq. (1)] and the percent removal [Eq. (2)] of boron were determined as follows:

$$q = \frac{\left(C_0 - C_e\right)}{m} \times V \tag{1}$$

$$\%\ \text{Removal of boron} = \frac{C_0 - C_e}{C_0} \times 100 \tag{2}$$

where C_0 is the initial boron concentration (mg/L), C_e is the boron concentration at equilibrium (mg/L), V is the volume of solution (L), m is the mass of UiO-66-NH_2 (g), and q is the adsorption capacity (mg/g).

2.5. Adsorption kinetics

In order to evaluate the adsorption kinetics of boron on UiO-66-NH_2, the effect of contact time on the boron adsorption capacity of UiO-66-NH_2 was studied at 10, 20, 30, 40, 50, 60, 120, 240, 360, and 420 min. In this experiment, the initial adsorbate concentration, adsorbent dose, temperature, and pH were controlled at 2 mg/L, 60 mg/L, 27°C, and 6, respectively. The pseudo-first-order [Eq. (3)], pseudo-second-order [Eq. (4)], and intraparticle diffusion [Eq. (5)] were applied to fit the experimental data. In addition, the accuracy of these models was evaluated by determining the nonlinear coefficient (R^2). The equations can be expressed as follows:

$$\ln\left(q_e - q_t\right) = \ln q_e - k_1 t \tag{3}$$

$$\frac{t}{q_t} = \frac{1}{k_2 q_e^2} + \frac{t}{q_e} \tag{4}$$

$$q_t = k_p \cdot t^{\frac{1}{2}} + C \tag{5}$$

where q_e is the amount adsorbed at equilibrium (mg/g), q_t is the amount adsorbed at any time t (mg/g), t is the adsorption time (minutes), k_1 is the rate constant (min^{-1}), k_2 is the second-order rate constant (g/mg min), k_p is the intraparticle diffusion rate constant (mg/g $min^{1/2}$), and C is the boundary layer thickness.

2.6. Adsorption isotherm

In the study of the adsorption isotherm, the initial concentration of boron ranged from 50 to 2,000 mg/L. The contact time, adsorbent dose, temperature, and pH in this experiment were controlled at 420 min, 60 mg/L, 27°C, and 6, respectively. Langmuir [Eq. (6)] and Freundlich [Eq. (7)] models were used to fit the experimental data. In addition, the accuracy of these models was evaluated by determining the nonlinear coefficient (R^2). The equations can be expressed as follows:

$$\frac{C_e}{q_e} = \frac{1}{q_m K_L} + \frac{C_e}{q_m} \tag{6}$$

$$\ln q_e = \ln K_F + \frac{1}{n} \ln C_e \tag{7}$$

where C_e is the equilibrium concentration (mg/L), q_e is the amount adsorbed at equilibrium (mg/g), q_m is the maximum concentration corresponding to a monolayer (mg/g), K_L is the Langmuir adsorption constant (L/mg), K_F is the Freundlich constant (mg/g(L/mg)$^{1/n}$), and n is the heterogeneity factor denoting the adsorption intensity.

2.7. Adsorption thermodynamics

Adsorption experiments were carried out at 27°C, 37°C, and 47°C in order to evaluate temperature effects. The thermodynamic parameters of the adsorption process such as Gibbs free energy change (ΔG), enthalpy change (ΔH), and entropy change (ΔS) can be calculated as follows:

$$\Delta G = -RT \ln K \tag{8}$$

$$\Delta G = \Delta G - T\Delta S \tag{9}$$

where R is the ideal gas constant (8.314 J/mol K), T is the absolute temperature (K), and K is the adsorption equilibrium constant obtained from the isotherms that have a better fitting parameter. The ΔH and ΔS values were obtained from the slope and intercept of the plot of ΔG vs. T.

2.8. Recycling of UiO-66-NH_2

The used UiO-66-NH_2 was stirred in 1 M HCl for 6 h at 27°C. Next, the UiO-66-NH_2 was washed 3 times with methanol and then dried in a vacuum at 80°C for 12 h. The regenerated UiO-66-NH_2 was reused for boron adsorption experiments and characterized using XRD and scanning electron microscopy (SEM). In this recycling experiment, the initial adsorbate concentration, adsorbent dose, contact time, pH, and temperature were controlled at 2 mg/L, 60 mg/L, 420 min, 6, and 27°C, respectively.

2.9. Optimization model with response surface methodology

Response surface methodology (RSM) is a set of mathematical and statistical techniques that are based on the establishment of polynomial equations for experimental data [33]. The equations must describe the behavior of datasets in order to make statistical predictions [34]. There were 3 parameters in this study: adsorbent dosage (X_1), pH (X_2), and temperature (X_3). Their randomized trials were run under the guidance of the Design-Expert version 8 (DX8) program (Table 1). The "response" of the model was the adsorption capacity (Y). Based on the interaction between independent parameters, the mathematical expression of boron adsorption on UiO-66-NH_2 was established and expressed as a second-order polynomial equation, as shown in Eq. (10):

$$Y = \beta_0 + \sum_{i=1}^{K}\beta_i X_i + \sum_{i=1}^{K}\beta_{ii}X_i^2 + \sum_{i=1}^{K-1}\sum_{j=1}^{K}\beta_{ii}X_iX_j \quad (10)$$

where Y is the predicted response, and X_i and X_j are the independent variables (i, j = 1, 2, 3, 4, …, k). The parameter β_0 is the offset coefficient, β_i is the linear coefficient, β_{ii} is the second-order coefficient, and β_{ij} is the interaction coefficient.

3. Results and discussion

3.1. Characteristics of UiO-66-NH_2

The XRD pattern of the prepared UiO-66-NH_2 (Fig. 1a) exhibited the same diffraction peaks and intensity as

Table 1
Experimental design levels of boron adsorption factors on UiO-66-NH_2

Factors	Code	Levels		
		–1	0	+1
Adsorbent dosage, mg/L	X_1	40	60	80
pH	X_2	5	6	7
Temperature, K	X_3	298	308	318

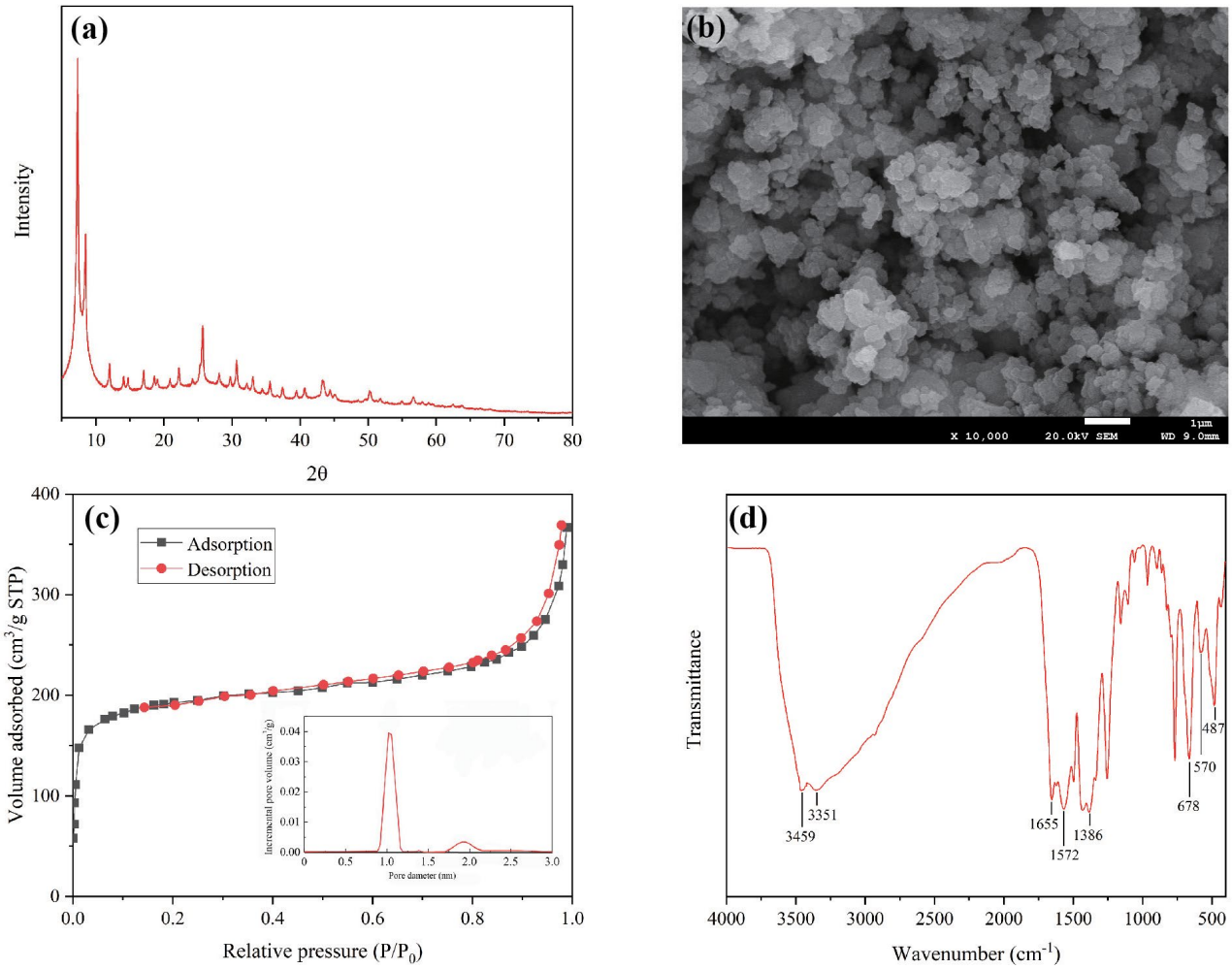

Fig. 1. (a) XRD pattern of the prepared UiO-66-NH_2, (b) SEM image of the prepared UiO-66-NH_2 at 10,000× magnification, (c) N_2 adsorption/desorption isotherms at 77 K (illustration is pore size distribution), and (d) FTIR spectra of the prepared UiO-66-NH_2.

previously reported [35]. The sharp diffraction peaks demonstrated that it has good crystallinity. The small differences in peak strength were due to changes in sample size and crystal orientation [36,37]. The SEM image of the prepared UiO-66-NH_2 at 10,000× magnification (Fig. 1b) revealed that it has a smooth surface and a clear cubic structure. Fig. 1c shows the corresponding curves of the pore size distribution (inset) for UiO-66-NH_2. UiO-66-NH_2 exhibited strictly type I isotherm with a predominantly microporous structure [38]. This is because the line type of the type I isotherm has a micropore filling feature characterized by a rapid rise in the adsorption volume at low relative pressures, followed by a flat phase before finally reaching a limit [39,40]. The specific surface area, pore-volume, and micropore volume of UiO-66-NH_2 are 831 m^2/g, 0.239 cm^3/g, and 0.217 cm^3/g, respectively. As shown in the FTIR spectra (Fig. 1d) of UiO-66-NH_2, the synergistic effect of the carboxyl group and Zr^{4+} is shown by the vibration peaks at 1,572 and 1,655 cm^{-1} [41]. The peaks at 1,482 and 1,382 cm^{-1} can be attributed to N-H bending vibration and C–N stretching vibration, respectively [42,43]. The symmetric and asymmetric stretching vibrations of N–H are at 3,351 and 3,459 cm^{-1}, respectively [32]. These characteristic peaks prove that the synthesis of UiO-66-NH_2 is effective. The particle size distribution (Fig. 2a) shows that the particle size of the prepared UiO-66-NH_2 ranged primarily between 500 and 700 nm, which is slightly larger than the previously reported results. This can be attributed to the difference of the DMF/Zr ratio in the preparation of UiO-66-NH_2 [44]. The change of zeta potential of UiO-66-NH_2 at different pH values (Fig. 2b) shows that the zeta potential is positive in the range of pH 4–5 and negative in the range of pH 6–10. Meanwhile, in the range of pH 4–5, the zeta potential rapidly increased from 35.3 to 41.1 mV, which was its maximum value. Then, as pH increased, it gradually decreased to its minimum value of 25.8 mV. The TG curve (Fig. 2c) shows that the weight loss below 200°C represents the loss of physically adsorbed water and solvent molecules in UiO-66-NH_2 [39,45]. The maximum weight loss of UiO-66-NH_2 was approximately 55% when the temperature reached 640°C.

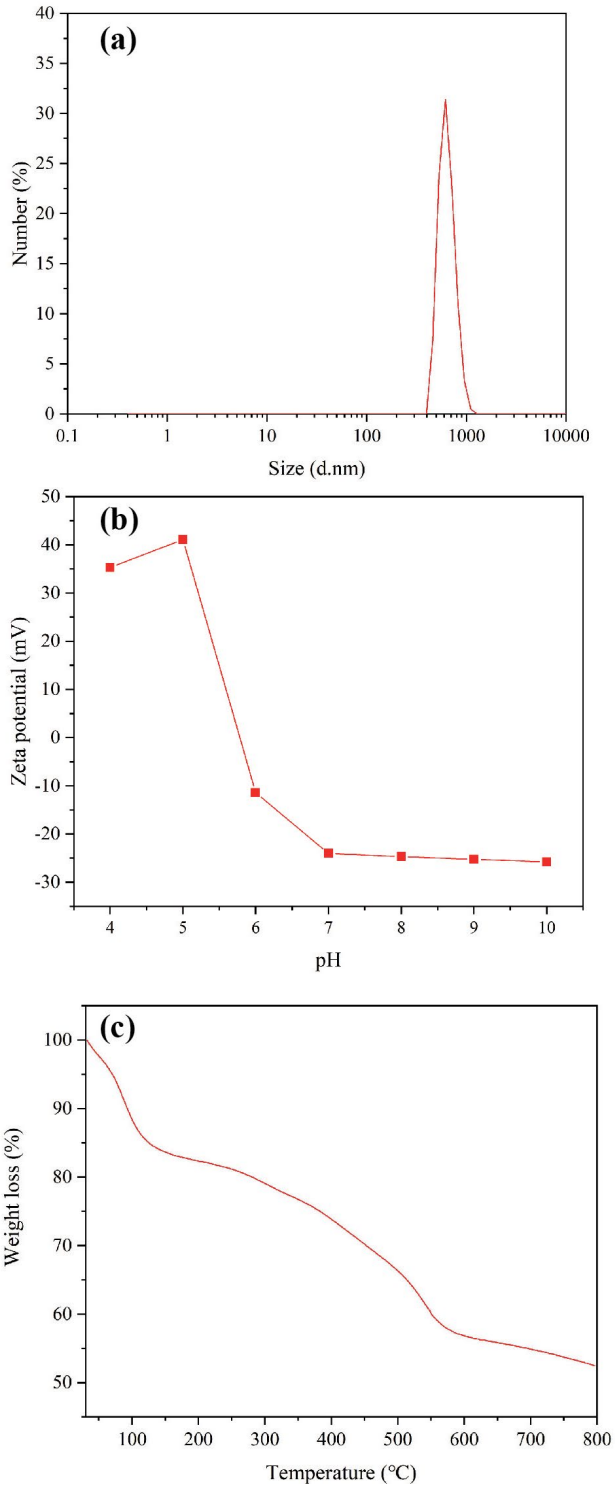

Fig. 2. (a) Particle size distribution of the prepared UiO-66-NH_2, (b) zeta potential of the prepared UiO-66-NH_2 at different pH values, and (c) TG curve of the prepared UiO-66-NH_2.

3.2. Effect of adsorbent dose on UiO-66-NH_2

The relationship between the adsorption capacity of UiO-66-NH_2 for boron and the adsorbent dosage is shown in Fig. 3a. As the dosage increased from 40 to 60 mg/L, the amount of boron adsorbed by UiO-66-NH_2 increased rapidly to 20.75 mg/g. This was mainly due to the increase of effective adsorption sites with an increase in adsorbent dosage. However, the amount of boron adsorbed by UiO-66-NH_2 tended to remain constant as the dosage increased to 120 mg/L. This may be due to the decrease of the concentration gradient between the adsorbate in solution and the adsorbate on the adsorbent surface, which leads to difficulties in aggregation and diffusion of adsorbate sites [46]. Given these results, 60 mg/L was used as the fixed absorbent dose in this study.

3.3. Effect of pH on UiO-66-NH_2

The change in the boron adsorption capacity of UiO-66-NH_2 at different initial pH values is shown in Fig. 3b. Obviously, the adsorption effect of UiO-66-NH_2 on boron is good when the pH is between 4 and 6. UiO-66-NH_2 exhibited the best adsorption of boron at pH = 5, when it reached 20.65 mg/g. However, as the pH increased from 7 to 10, the

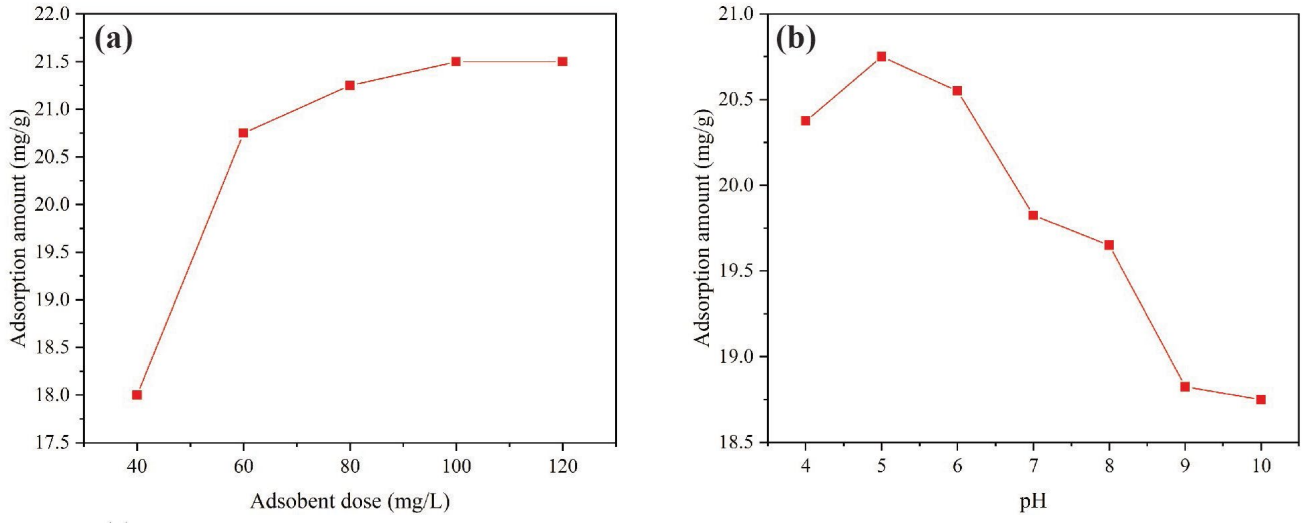

Fig. 3. (a) Effect of adsorbent dose on boron adsorption (temperature 298 K; pH 5; contact time 480 min; adsorbate concentration 2 mg L^{-1}) and (b) effect of pH on boron adsorption (temperature 298 K; adsorbent dose 60 mg L^{-1}; contact time 480 min; adsorbate concentration 2 mg L^{-1}).

UiO-66-NH_2 boron adsorption capacity decreased gradually. This is because boron exists in the form of $B(OH)_3$ or $B(OH)_4^-$ when the total concentration of boron is less than 25 mM [47]. When the pH value is between 4 and 6, boron mainly exists in the form of $B(OH)_3$. Therefore, the surface electrostatic effect of the adsorbent is not obvious. With the increase of pH from 6 to 10, $B(OH)_3$ gradually transforms into a $B(OH)_4^-$ structure. The electrostatic repulsion between $B(OH)_4^-$ and the negatively-charged adsorbent then results in the reduction of boron adsorption at high pH.

3.4. Effect of contact time and adsorption kinetics on UiO-66-NH_2

The effect of contact time on the adsorption of boron by UiO-66-NH_2 is shown in Fig. 4a. Since there were enough adsorption sites in UiO-66-NH_2 at the beginning of the adsorption test, the amount of boron adsorbed by UiO-66-NH_2 quickly reached 15.75 mg/g in the first 60 min. Following that, there was a slow adsorption process, which reached equilibrium by 420 min. This was due to the adsorption point saturation during the latter stages of the adsorption test. Under equilibrium conditions, the adsorption capacity of boron by UiO-66-NH_2 was found to be 20.75 mg/g.

In order to study the adsorption mechanism of boron on UiO-66-NH_2, the pseudo-first-order kinetic model (Fig. 4b) and the pseudo-second-order kinetic model (Fig. 4c) were introduced to investigate the adsorption process. The fitting data of the kinetic model are shown in Table 2. The R^2 value of the pseudo-first-order kinetic model was only 0.9569, indicating that the pseudo-first-order kinetic model is not suitable for the adsorption of boron by UiO-66-NH_2 [48]. In contrast, R^2 of the pseudo-second-order kinetic model was 0.9989, and the fitted $q_{e,cal}$ was closer to the experimental $q_{e,exp}$. These results indicate that the adsorption kinetic model of boron on UiO-66-NH_2 conforms to the pseudo-second-order model [49]. The pseudo-second-order model assumes that the adsorption rate is controlled by chemical adsorption [13]. This chemical adsorption involves electron covalence or electron migration between adsorbate and adsorbent [50].

In order to further understand the diffusion mechanism, the intraparticle diffusion model (Fig. 4d) was used to analyze the dynamics. The intraparticle diffusion process consists of 3 steps: mass transfer, adsorption, and diffusion [51]. In this study, the adsorption process (stage 1) and the diffusion process (stage 2) were the main steps of intraparticle diffusion, since the mass transfer process was completed in a short time. The slope and correlation coefficient (R^2) of the first and second stages were 2.3706 and 0.4144; 0.9944 and 0.9918, respectively. The adsorption rate of boron on the UiO-66-NH_2 pore was higher than that of the boron intraparticle diffusion in the particle. At the same time, the fitting line did not cross the origin, indicating that intraparticle diffusion was not the only rate control step.

3.5. Effect of initial concentration and adsorption isotherm on UiO-66-NH_2

The effect of initial concentration on the adsorption of boron by UiO-66-NH_2 is shown in Fig. 5a. It can be seen that the adsorption increases with increasing boron solution concentration from 2 to 100 mg/L. This can be explained by the fact that the initial increase of boron concentration provides a driving force for overcoming mass transfer resistance [52,53]. This phenomenon shows that UiO-66-NH_2 still exhibits a good adsorption effect on boron at high concentrations. Thus, UiO-66-NH_2 has potential applications in industrial boron removal.

The study of adsorption isotherms is helpful for understanding the interaction between adsorbates and adsorbents. The fitting curves of the Langmuir and Freundlich models are shown in Figs. 5b and c, respectively. The fitting parameters are listed in Table 3. Based on the correlation

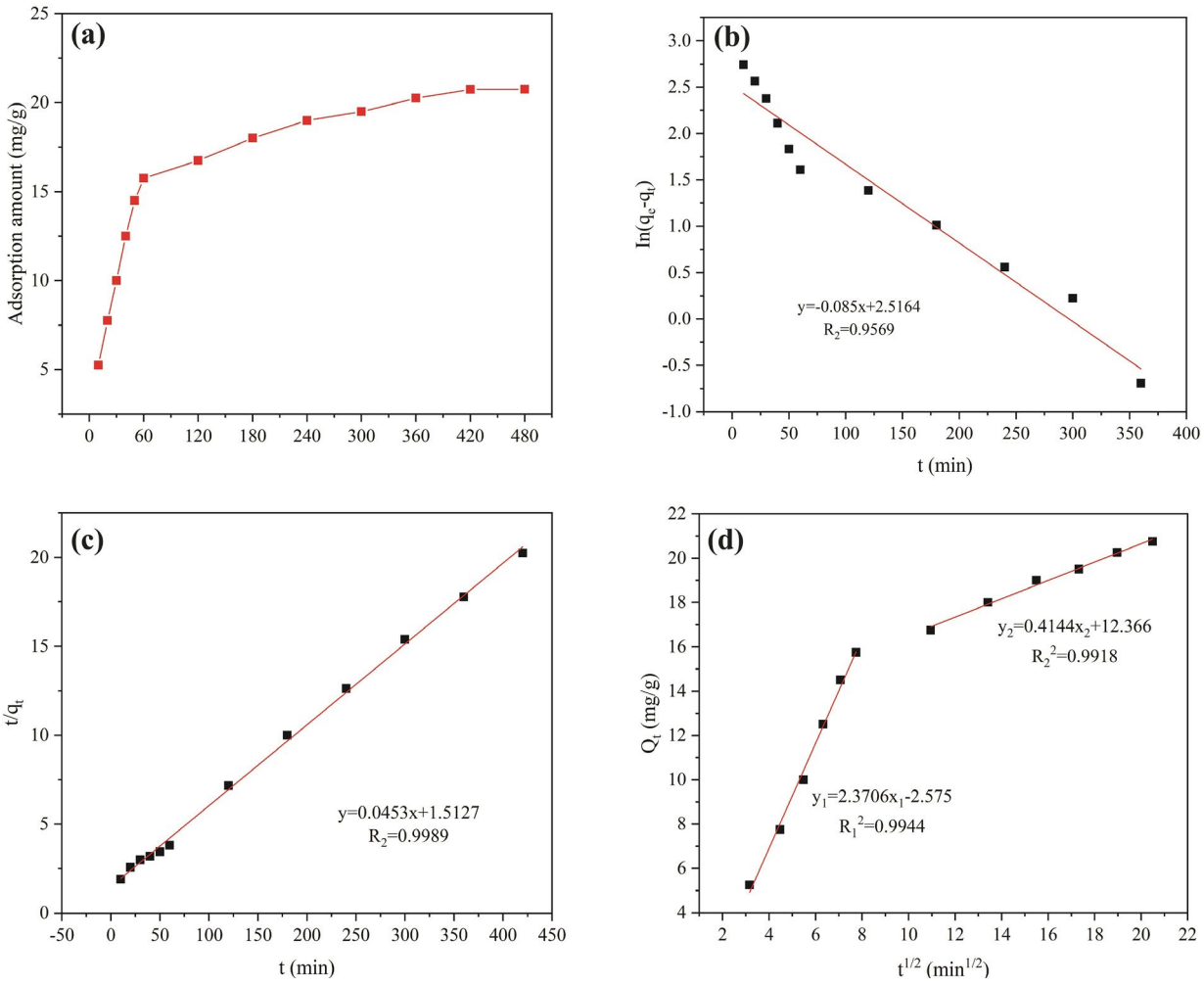

Fig. 4. (a) Effect of contact time on boron adsorption (temperature 298 K; pH 5; adsorbent dose 60 mg L^{-1}; adsorbate concentration 2 mg L^{-1}), (b) pseudo-first-order kinetic model of boron on UiO-66-NH_2, (c) pseudo-second-order kinetic model of boron on UiO-66-NH_2, and (d) intraparticle diffusion model of boron on UiO-66-NH_2.

Table 2
Kinetic constants of boron adsorption on UiO-66-NH_2

Kinetic models	Parameters	Value
Pseudo-first-order model	$q_{e,exp}$ (mg/g)	20.75
	$q_{e,cal}$ (mg/g)	12.38
	k_1 (min^{-1})	0.0085
	R^2	0.9569
Pseudo-second-order model	$q_{e,exp}$ (mg/g)	20.75
	$q_{e,cal}$ (mg/g)	22.08
	k_2 (min^{-1})	0.0013
	R^2	0.9989
Intraparticle diffusion model	k_{p1} (mg/g $min^{1/2}$)	2.3796
	C_1	–2.575
	R_1^2	0.9944
	k_{p2} (mg/g $min^{1/2}$)	0.4144
	C_2	12.366
	R_2^2	0.9783

coefficient (R^2), the Langmuir model can better describe the adsorption of boron on UiO-66-NH_2 than the Freundlich model. This indicates that the adsorption of boron on UiO-66-NH_2 is a monolayer [54]. The maximum adsorption capacity of UiO-66-NH_2 for boron was found to be 188.67 mg/g, demonstrating a high boron adsorption capacity.

3.6. Adsorption thermodynamics

The study of thermodynamics is helpful for understanding the type and mechanism of the adsorption process [55]. The calculated values of ΔG, ΔH, and ΔS are summarized in Table 4. The value of ΔG is negative and decreases with increasing temperature. This indicates that the adsorption of boron is spontaneous. The higher the temperature, the better the adsorption of boron by UiO-66-NH_2. The positive ΔH value indicates that the adsorption of boron by UiO-66-NH_2 is an endothermic process. The positive ΔS reveals that UiO-66-NH_2 has a good affinity for boron. At the same time, it also shows that the randomness of the solid–liquid interface increases during the adsorption process [56].

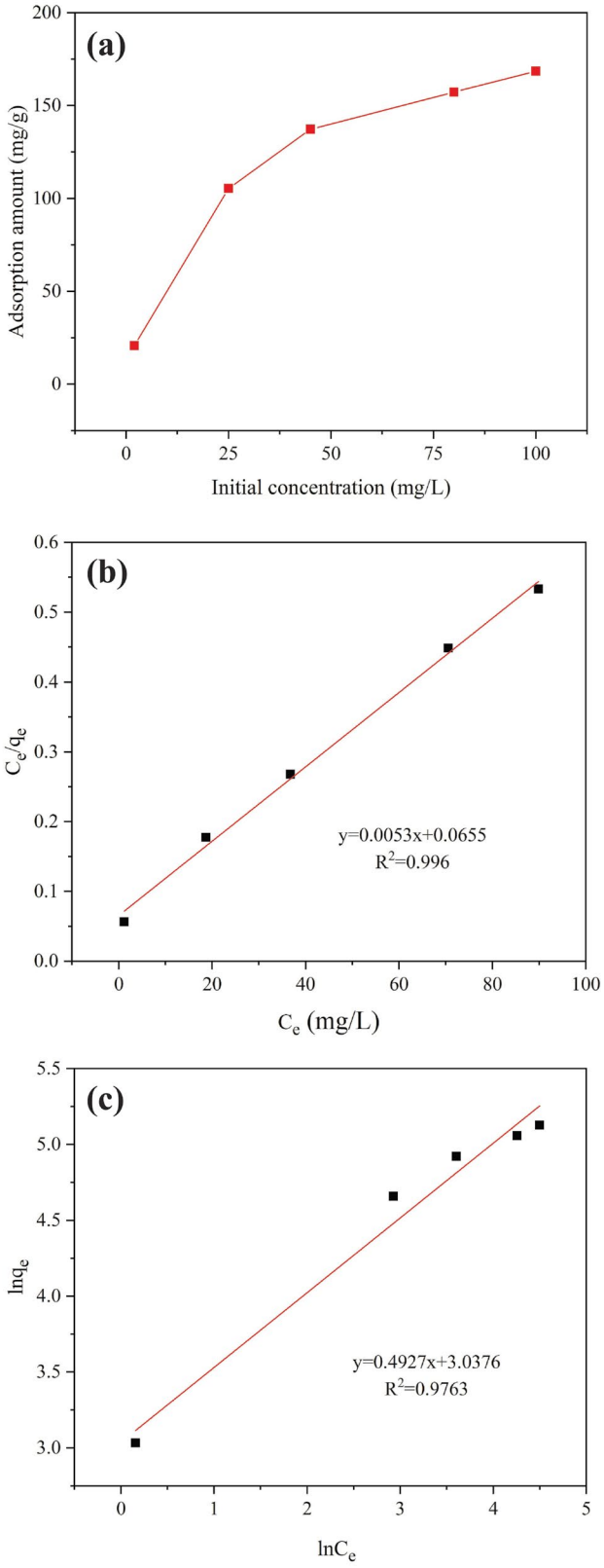

Fig. 5. (a) Effect of initial concentration on boron adsorption (temperature 298 K; pH 5; adsorbent dose 60 mg L^{-1}; contact time 480 min), (b) Langmuir model of boron on UiO-66-NH_2, and (c) Freundlich model of boron on UiO-66-NH_2.

Table 3
Parameters for Langmuir and Freundlich models of boron adsorption on UiO-66-NH_2

Isotherm models	Constant	Value
Langmuir model	q_m (mg/g)	188.67
	K_L (L/mg)	0.08
	R^2	0.996
Freundlich model	n	2.03
	K_F	20.84
	R^2	0.9763

Table 4
Adsorption thermodynamic parameters of boron adsorption on UiO-66-NH_2

T (K)	ΔG (kJ/mol)	ΔH (kJ/mol)	ΔS (kJ/(mol K))
298	–16.1341		
308	–17.4576	16.454	0.1096
318	–18.3263		

3.7. Reusability of UiO-66-NH_2

In order to explore the reusability of UiO-66-NH_2, 3 successive cycles of adsorption experiments were performed. As can be seen in Fig. 6a, the adsorption amount of boron by UiO-66-NH_2 decreased by 6% after 3 cycles. This indicates that the adsorption of boron by UiO-66-NH_2 was still stable. The SEM and XRD diagrams of UiO-66-NH_2 after 3 regeneration cycles are shown in Figs. 6b and c, respectively. Compared with the original synthesis of UiO-66-NH_2, there was no significant change. This shows that regeneration has no obvious effect on the crystal structure of UiO-66-NH_2.

3.8. Optimization of the boron adsorption capacity of UiO-66-NH_2 by RSM

The Box–Behnken experimental design and results of UiO-66-NH_2 adsorption of boron are shown in Table 5. The experimental data were used to calculate the predictive response of the software. The quadratic polynomial relationship between the experimental response and the independent variable is shown in Eq. (11):

$$Y = 22.71 + 1.72X_1 - 0.48X_2 + 1.41X_3 - 0.04X_1X_2 + 0.16X_1X_3 - 0.032X_2X_3 - 1.27X_1^2 - 0.4X_2^2 - 0.55X_3^2. \quad (11)$$

The synergistic efficiency of the analysis of variance data is listed in Table 6, including the sum of squares, degree of freedom, mean square, F-value, and P-value. The variance analysis results demonstrate that the F-value is high and acceptable, while the P-value is low and acceptable. This shows that the proposed quadratic model has statistical significance [57]. Fig. 7a presents the normal

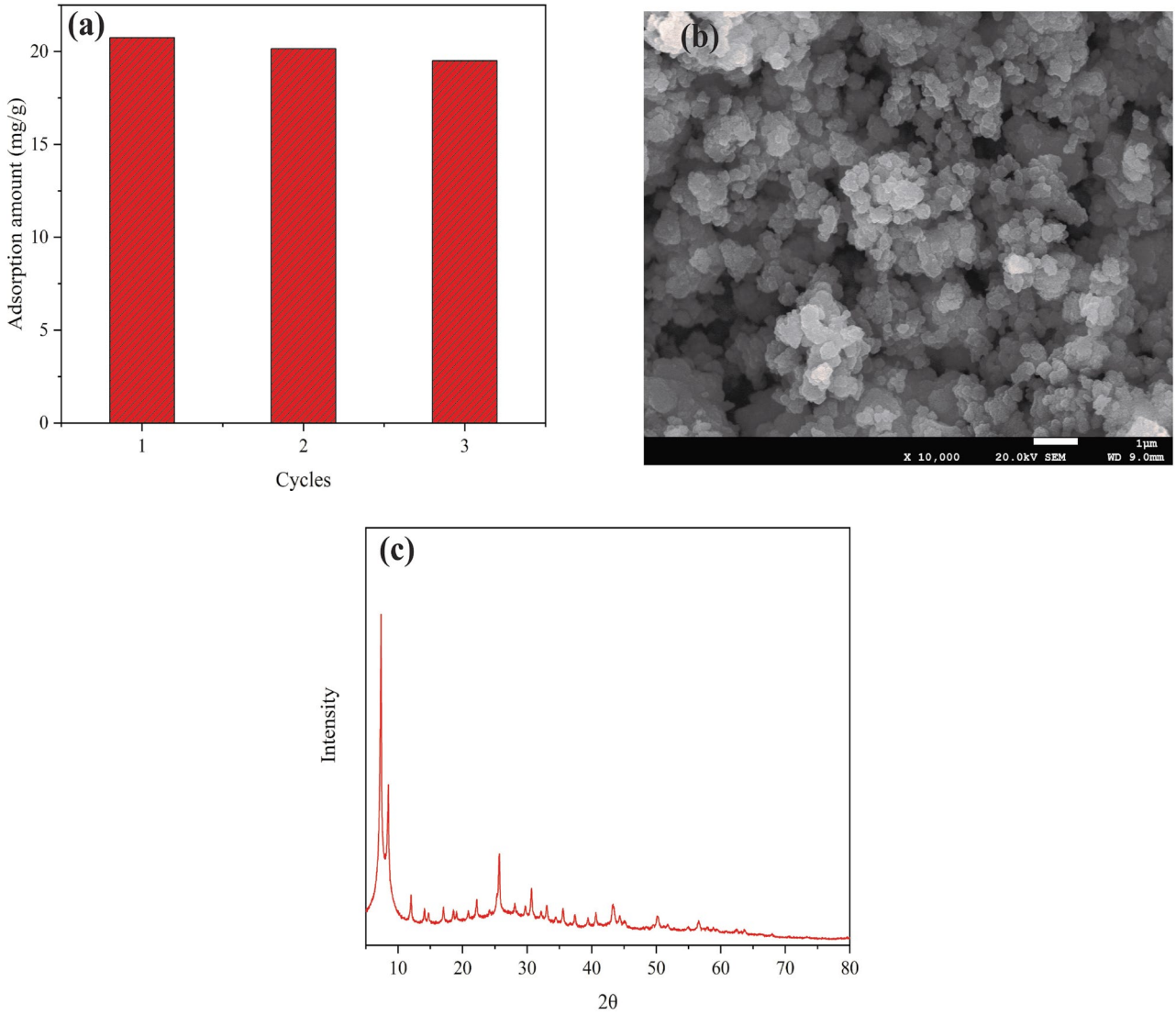

Fig. 6. (a) Boron adsorption capacity of three reuse cycles, (b) SEM image of UiO-66-NH_2 after three regeneration cycles, and (c) XRD pattern of UiO-66-NH_2 after three regeneration cycles.

distribution of the internal research residuals for process response. From this linear profile, it can be seen that the variance did not change greatly, indicating that the prediction model has a high degree of fitting [58]. Fig. 7b shows the abnormal curve of boron adsorption on UiO-66-NH_2. It is not difficult to see that the residuals of the internally studentized data were randomly distributed in all experimental runs. All of the experimental data fell within the range of –2 to +2, and no abnormal values were detected. It can be concluded that the model prediction was accurate [59]. Fig. 8 shows the three-dimensional response surface, which reveals the uniform influence of the 3 factors on the boron adsorption efficiency of UiO-66-NH_2. Generally speaking, the increase of adsorbent dosage, the decrease of solution pH, and the increase of temperature are beneficial to the adsorption process of boron. This is consistent with the previous experimental results. Therefore, the optimum conditions for maximum boron adsorption are dosage > 80 mg/L, pH < 5, and temperature > 318 K. Based on the model, the following optimum conditions were obtained: adsorbent dosage = 75.49 mg/L, pH = 5.3, and temperature = 322.11 K. The predicted maximum adsorption capacity of boron was 24.54 mg/g. In order to verify the accuracy and confidence of the proposed optimization conditions, verification experiments were carried out using the above conditions. The experimental verification revealed that under the optimum conditions, the deviation between the predicted value and the measured value (25.13 mg/g) was 2.4%. This indicates that the optimization model of boron adsorption on UiO-66-NH_2 is highly compatible and can be used to design and optimize experimental conditions. A comparison of different boron adsorption materials is shown in Table 7. Obviously, UiO-66-NH_2 has a more prominent boron adsorption capacity.

Table 5
Results of Box–Behnken design on the adsorption of boron by UiO-66-NH_2

Run	Factor (input variables)			Response variable	
	X_1	X_2	X_3	q_{exp} (mg/g)	q_{pred} (mg/g)
1	0	–1	1	23.75	23.69
2	–1	1	0	18.86	18.88
3	0	0	0	22.75	22.71
4	1	1	0	22.27	22.23
5	0	1	1	22.7	22.66
6	–1	0	1	20.4	20.42
7	0	0	0	20.74	22.71
8	0	–1	–1	20.75	20.80
9	1	0	–1	21.05	21.03
10	0	0	0	22.69	22.71
11	0	1	–1	19.83	19.89
12	0	0	0	22.6	22.71
13	0	0	0	22.77	22.71
14	1	0	1	24.09	24.17
15	1	–1	0	23.3	23.28
16	–1	0	–1	18	17,82
17	–1	–1	0	19.73	19.77

Table 6
Analysis of variance data for the boron adsorption model

Source	Sum of squares	Freedom degree	Mean square	*F*-value	*P*-value
Model	50.99	9	5.67	800.86	<0.0001
X_1	23.53	1	23.53	3,325.77	<0.0001
X_2	1.87	1	1.87	264.61	<0.0001
X_3	15.99	1	15.99	2,260.00	<0.0001
X_1X_2	14.39	1	14.39	0.90	0.3732
X_1X_3	0.10	1	0.10	14.47	0.0067
X_2X_3	8.48	1	8.48	0.60	0.4649
$(X_1)^2$	6.80	1	6.80	961.77	<0.0001
$(X_2)^2$	0.67	1	0.67	94.63	<0.0001
$(X_3)^2$	1.29	1	1.29	182.49	<0.0001

Table 7
Comparison of boron adsorption for different materials

Adsorbent	Adsorption capacity (mg/g)	pH	Temperature (k)	Time (h)	C_0 (mg/L)	Reference
Zirconium-chitosan hydrogel bead	24.5	7	298	48	500	[60]
Modified activated carbon	1.5	8.5	298	4	60	[61]
CA@KH-550@EPH@NMDG	15.62	9.5	298	15	440	[62]
Few-layer hydrotalcite nanosheet	6.2	7–8	298	15	25	[63]
Pyrocatechol modified resin	4.54	9	298	12	22	[64]
Calcined magnesite tailing	36.3	6	318	7	67	[65]
UiO-66-NH_2	25.13	5.3	322	14.47	7	This study

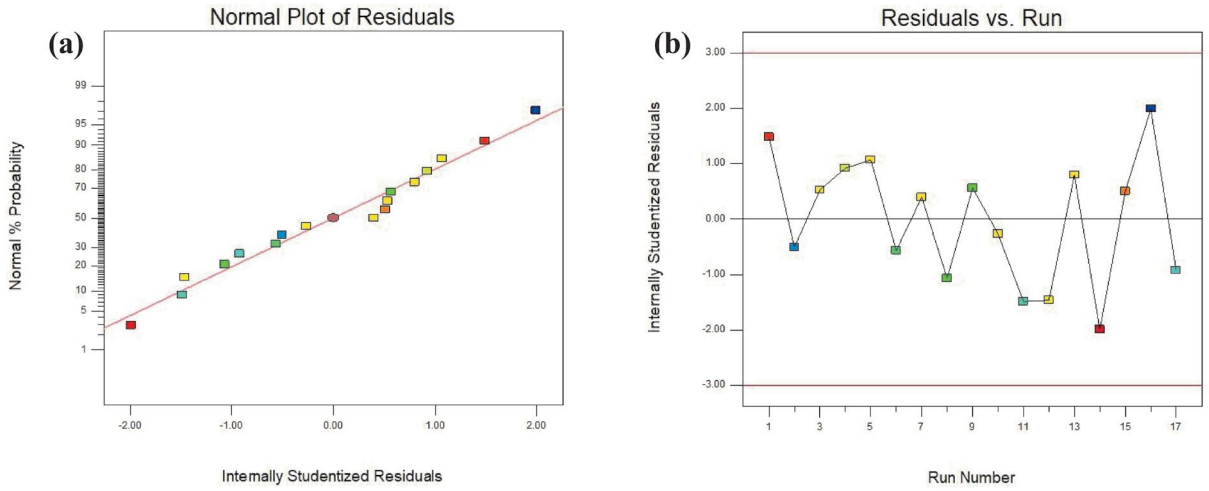

Fig. 7. (a) Internally studentized plot and (b) internally studentized plot vs. run plot.

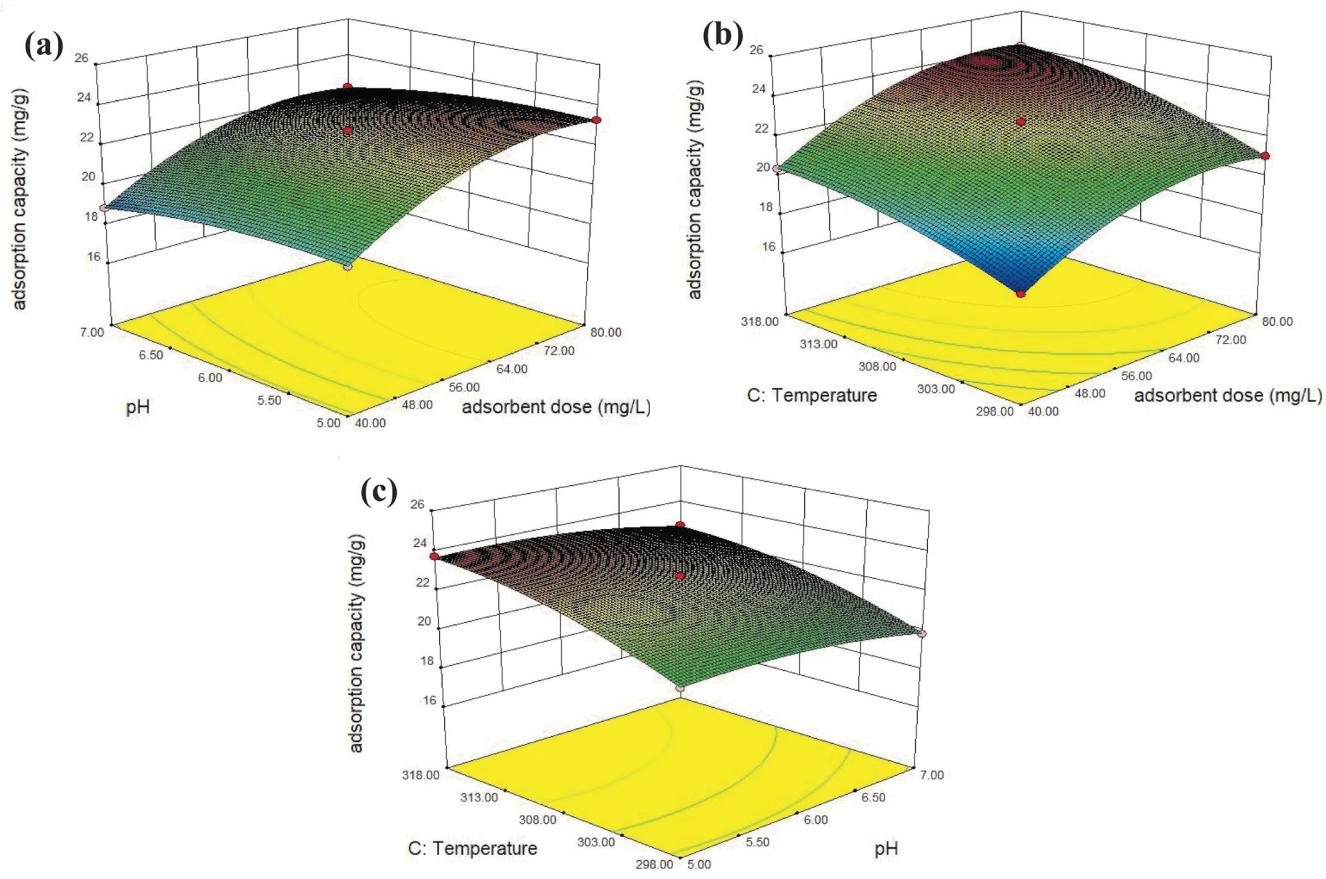

Fig. 8. (a) Effect of adsorbent dose and pH on boron adsorption (temperature 308 K; adsorbate concentration 2 mg L^{-1}; contact time 480 min), (b) effect of adsorbent dose and temperature on boron adsorption (pH 6; adsorbate concentration 2 mg L^{-1}; contact time 480 min), and (c) effect of pH and temperature on boron adsorption (adsorbent dose 60 mg L^{-1}; adsorbate concentration 2 mg L^{-1}; contact time 480 min).

4. Conclusions

In this study, the adsorption behavior of boron in desalinated seawater by UiO-66-NH_2 was investigated. The RSM method was used for optimization. The optimum adsorbent dosage, pH, and temperature were found to be 75.49 mg/L, 5.3, and 322.11 K, respectively. Under these conditions, the model-fitting adsorption capacity of boron (24.54 mg/g) was close to the actual value (25.13 mg/g). The optimization model can thus be used to design and optimize experimental conditions. Kinetic and isotherm models revealed that the adsorption process follows the chemical adsorption and monolayer behavior mechanisms. The thermodynamic parameters demonstrated that the adsorption of boron by UiO-66-NH_2 is spontaneous and feasible. UiO-66-NH_2 has a higher adsorption capacity than amberlite IRA-743. In addition, it also exhibits good regeneration performance. UiO-66-NH_2 shows great potential for use in boron removal after seawater desalination.

Acknowledgment

The authors express their sincere gratitude to the National Key Research and Development Program of China (No. 2018YFC0408000, 2018YFC0408004).

References

[1] H.Q. Xue, T. Yang, X.D. Liu, S. Wu, Analysis of heavy metal contamination in urban road-deposited sediments in Nanjing, China, Fresenius Environ. Bull., 27 (2018) 6661–6667.
[2] L. Gao, S. Yoshikawa, Y. Iseri, S. Fujimori, S. Kanae, An economic assessment of the global potential for seawater desalination to 2050, Water, 9 (2017) 763.
[3] N. Kabay, E. Güler, M. Bryjak, Boron in seawater and methods for its separation — a review, Desalination, 261 (2010) 212–217.
[4] WHO, Guidelines for Drinking-Water Quality, 4th ed., World Health Organization, Switzerland, 2011.
[5] N. Geffen, R. Semiat, M.S. Eisen, Y. Balazs, I. Katz, C.G. Dosoretz, Boron removal from water by complexation to polyol compounds, J. Membr. Sci., 286 (2006) 45–51.
[6] O.C. Türker, A. Yakar, C. Türe, Ç. Saz, Cost-effectiveness of boron (B) removal from irrigation water: an economic water treatment model (EWTM) for farmers to prevent boron toxicity, Environ. Sci. Pollut. Res., 26 (2019) 18777–18789.
[7] X.R. Nan, J. Liu, X.L. Wang, X.H. Pan, X.M. Wang, X. Zhang, Preparation of superhydrophilic adsorbents with 3DOM structure by water-soluble colloidal crystal templates for boron removal from natural seawater, ACS Appl. Mater. Interfaces, 10 (2018) 36918–36925.
[8] B.-Y. Cho, H.-W. Kim, Y.-S. Shin, A study on boron removal for seawater desalination using the combination process of mineral cluster and RO membrane system, Environ. Eng. Res., 20 (2015) 285–289.
[9] Y.K. Bang, C. Park, J.H. Han, T.J. Lee, Y. Choi, H.I. Kim, Synthesis of modified chelate resins containing N-methyl-D-glucamine and improvement of boron removing characteristics, Polymer-Korea, 42 (2018) 409–416.
[10] M.A. Myachina, Y.A. Polyakova, N.N. Gavrilova, V.V. Nazarov, V.A. Kolesnikov, ZrO_2–carbon nanotubes composite sorbent for treatment of aqueous solutions to remove boron, Russ. J. Appl. Chem., 90 (2017) 895–900.
[11] D. Kartikaningsih, Y.-H. Huang, Y.-J. Shih, Electro-oxidation and characterization of nickel foam electrode for removing boron, Chemosphere, 166 (2017) 184–191.
[12] A.V. Desyatov, V.A. Kolesnikov, N.E. Kruchinina, A.M. Landyrev, A.V. Kolesnikov, Two-level scheme for removing boron compounds during the desalinating of seawater by reverse osmosis, Theor. Found. Chem. Eng., 49 (2015) 370–374.
[13] Z.Q. Jing, Y.Y. Peng, R. He, Y. Xu, T. Yu, J. Hu, Poplar leaves reclamation for porous granules and their application in nitrobenzene removal from aqueous solution, Desal. Water Treat., 57 (2016) 449–458.
[14] E.B. Simsek, U. Beker, B.F. Senkal, Predicting the dynamics and performance of selective polymeric resins in a fixed bed system for boron removal, Desalination, 349 (2014) 39–50.
[15] İ.Y. İpek, N. Kabay, M. Yüksel, Modeling of fixed bed column studies for removal of boron from geothermal water by selective chelating ion exchange resins, Desalination, 310 (2013) 151–157.
[16] T. Chen, Q.F. Wang, J.F. Lyu, P. Bai, X.H. Guo, Boron removal and reclamation by magnetic magnetite (Fe_3O_4) nanoparticle: an adsorption and isotopic separation study, Sep. Purif. Technol., 231 (2020) 115930.
[17] X.-Y. Chen, F.-Z. Teng, D.C. Catling, Fast and precise boron isotopic analysis of carbonates and seawater using Nu Plasma II multi-collector inductively coupled plasma mass spectrometry and a simple sample introduction system, Rapid Commun. Mass Spectrom., 33 (2019) 1169–1178.
[18] Y.N. Bian, N.N. Xiong, G.C. Zhu, Technology for the remediation of water pollution: a review on the fabrication of metal organic frameworks, Processes, 6 (2018) 112.
[19] K. Rui, X.S. Wang, M. Du, Y. Zhang, Q.Q. Wang, Z.Y. Ma, Q. Zhang, D.S. Li, X. Huang, G.Z. Sun, J.X. Zhu, W. Huang, Dual-function metal–organic framework-based wearable fibers for gas probing and energy storage, ACS Appl. Mater. Interfaces, 10 (2018) 2837–2842.
[20] M. Zhang, L. Ma, L.L. Wan, Y.W. Sun, Y. Liu, Insights into the use of metal-organic framework as high-performance anticorrosion coatings, ACS Appl. Mater. Interfaces, 10 (2018) 2259–2263.
[21] L. Joseph, B.-M. Jun, M. Jang, C.M. Park, J.C. Muñoz-Senmache, A.J. Hernández-Maldonado, A. Heyden, M. Yu, Y.M. Yoon, Removal of contaminants of emerging concern by metal-organic framework nanoadsorbents: a review, Chem. Eng. J., 369 (2019) 928–946.
[22] J.-D. Xiao, H.-L. Jiang, Metal-organic frameworks for photocatalysis and photothermal catalysis, Acc. Chem. Res., 52 (2019) 356–366.
[23] F.K. Bi, X.D. Zhang, J.F. Chen, Y. Yang, Y.X. Wang, Excellent catalytic activity and water resistance of UiO-66-supported highly dispersed Pd nanoparticles for toluene catalytic oxidation, Appl. Catal., B, 269 (2020) 118767.
[24] J. Wang, P.P. Han, Y. Xia, A cationic metal-organic framework for the highly efficient removal of thiocyanate from water, Microporous Mesoporous Mater., 287 (2019) 107–113.
[25] S.-Y. Fang, P. Zhang, J.-L. Gong, L. Tang, G.-M. Zeng, B. Song, W.-C. Cao, J. Li, J. Ye, Construction of highly water-stable metal-organic framework UiO-66 thin-film composite membrane for dyes and antibiotics separation, Chem. Eng. J., 385 (2020) 123400.
[26] J. Li, Q.Y. Duan, Z. Wu, X. Li, K. Chen, G. Song, A. Alsaedi, T. Hayat, C.L. Chen, Few-layered metal-organic framework nanosheets as a highly selective and efficient scavenger for heavy metal pollution treatment, Chem. Eng. J., 383 (2020) 123189.
[27] R. Pei, L.L. Fan, F.G. Zhao, J. Xiao, Y.C. Yang, A. Lai, S.-F. Zhou, G. Zhan, 3D-Printed metal-organic frameworks within biocompatible polymers as excellent adsorbents for organic dyes removal, J. Hazard. Mater., 384 (2020) 121418–121418.
[28] X.X. Wang, S.J. Yu, X.K. Wang, Removal of radionuclides by metal-organic framework-based materials, J. Inorg. Mater., 34 (2019) 17–26.
[29] X.X. Wang, L. Chen, L. Wang, Q.H. Fan, D.Q. Pan, J.X. Li, F.T. Chi, Y. Xie, S.J. Yu, C.L. Xiao, F. Luo, J. Wang, X.L. Wang, C.L. Chen, W.S. Wu, W.Q. Shi, S. Wang, X.K. Wang, Synthesis of novel nanomaterials and their application in efficient removal of radionuclides, Sci. China-Chem., 62 (2019) 933–967.
[30] L.K. Fu, S.X. Wang, G. Lin, L.B. Zhang, Q.M. Liu, H.H. Zhou, C.X. Kang, S.Y. Wan, H.W. Li, S. Wen, Post-modification of UiO-66-NH_2 by resorcyl aldehyde for selective removal of Pb(II) in aqueous media, J. Cleaner Prod., 229 (2019) 470–479.

[31] S.B. Wu, Y.J. Ge, Y.Q. Wang, X. Chen, F.F. Li, H. Xuan, X. Li, Adsorption of Cr(VI) on nano UiO-66-NH_2 MOFs in water, Environ. Technol., 39 (2018) 1937–1948.
[32] Y.X. Fang, L.X. Zhang, Q.Q. Zhao, X.L. Wang, X. Jia, Application of acid-promoted UiO-66-NH_2 MOFs in the treatment of wastewater containing methylene blue, Chem. Pap., 73 (2019) 1401–1411.
[33] J.D. Castro-Castro, N.R. Sanabria-González, G.I. Giraldo-Gómez, Experimental data of adsorption of Cr(III) from aqueous solution using a bentonite: optimization by response surface methodology, Data Brief, 28 (2020) 105022–105022.
[34] M.A. Bezerra, R.E. Santelli, E.P. Oliveira, L.S. Villar, L.A. Escaleira, Response surface methodology (RSM) as a tool for optimization in analytical chemistry, Talanta, 76 (2008) 965–977.
[35] J. Yang, L. Yang, H.L. Ye, F.Q. Zhao, B.Z. Zeng, Highly dispersed AuPd alloy nanoparticles immobilized on UiO-66-NH_2 metal-organic framework for the detection of nitrite, Electrochim. Acta, 219 (2016) 647–654.
[36] Q. Liang, M. Zhang, Z.H. Zhang, C.H. Liu, S. Xu, Z.Y. Li, Zinc phthalocyanine coupled with UIO-66 (NH_2) via a facile condensation process for enhanced visible-light-driven photocatalysis, J. Alloys Compd., 690 (2017) 123–130.
[37] L. Wang, G.Y. Yin, Y.Q. Yang, X.D. Zhang, Enhanced CO oxidation and toluene oxidation on CuCeZr catalysts derived from UiO-66 metal organic frameworks, React. Kinet. Mech. Catal., 128 (2019) 193–204.
[38] X.D. Zhang, X.Y. Shi, J.F. Chen, Y. Yang, G. Lu, The preparation of defective UiO-66 metal organic framework using MOF-5 as structural modifier with high sorption capacity for gaseous toluene, J. Environ. Chem. Eng., 7 (2019) 103405.
[39] S.H. Lin, T.T. Zhou, S.S. Yin, Properties of thermally treated granular montmorillonite-palygorskite adsorbent (GMPA) and use to remove Pb^{2+} and Cu^{2+} from aqueous solutions, Clays Clay Miner., 65 (2017) 184–192.
[40] X.D. Zhang, L. Song, F.K. Bi, D.F. Zhang, Y.X. Wang, L.F. Cui, Catalytic oxidation of toluene using a facile synthesized Ag nanoparticle supported on UiO-66 derivative, J. Colloid Interface Sci., 571 (2020) 38–47.
[41] Y.R. Du, X.Q. Li, X.J. Lv, Q. Jia, Highly sensitive and selective sensing of free bilirubin using metal–organic frameworks-based energy transfer process, ACS Appl. Mater. Interfaces, 9 (2017) 30925–30932.
[42] M. Kandiah, S. Usseglio, S. Svelle, U. Olsbye, K.P. Lillerud, M. Tilset, Post-synthetic modification of the metal-organic framework compound UiO-66, J. Mater. Chem., 20 (2010) 9848–9851.
[43] G.H. Liu, S.H. Lin, L.S. Pile, Z. Fang, G.G. Wang, Effect of potassium permanganate and pyrolysis temperature on the biochar produced from rice straw and suitability of biochars for heavy metal (CD & PB) immobilization in paper sludge, Fresenius Environ. Bull., 27 (2018) 9008–9018.
[44] Z.-W. Chang, Y.-J. Lee, D.-J. Lee, Adsorption of hydrogen arsenate and dihydrogen arsenate ions from neutral water by UiO-66-NH_2, J. Environ. Manage., 247 (2019) 263–268.
[45] X.D. Zhang, Y. Yang, W.Y. Huang, Y.Q. Yang, Y.X. Wang, C. He, N. Liu, M.H. Wu, L. Tang, g-C_3N_4/UiO-66 nanohybrids with enhanced photocatalytic activities for the oxidation of dye under visible light irradiation, Mater. Res. Bull., 99 (2018) 349–358.
[46] R.M. Gong, Y. Ding, H.J. Liu, Q.Y. Chen, Z.L. Liu, Lead biosorption and desorption by intact and pretreated *spirulina maxima* biomass, Chemosphere, 58 (2005) 125–130.
[47] Q. Wu, M.Y. Liu, X. Wang, A novel chitosan based adsorbent for boron separation, Sep. Purif. Technol., 211 (2019) 162–169.
[48] J.-J. Lian, M. Yang, S.-S. Wang, B. Chen, F.-J. Zhou, Z.-L. Liu, Treatment of molybdenum(VI)-containing groundwater using chitosan nanoparticle: adsorption mechanism and performances, Desal. Water Treat., 167 (2019) 258–268.
[49] X.L. Zhang, X.M. Song, Adsorption of chromium (VI) and phosphorous (V) from aqueous solution by calcined Mg–Al–CO_3 hydrotalcite-like compound, Desal. Water Treat., 163 (2019) 190–197.
[50] L.K. Fu, S.X. Wang, G. Lin, L.B. Zhang, Q.M. Liu, J. Fang, C.H.N. Wei, G. Liu, Post-functionalization of UiO-66-NH_2 by 2,5-Dimercapto-1,3,4-thiadiazole for the high efficient removal of Hg(II) in water, J. Hazard. Mater., 368 (2019) 42–51.
[51] M. Hajilari, A. Shariati, M. Khosravi-Nikou, Mass transfer determination of ethanol adsorption on activated carbon: kinetic adsorption modeling, Heat Mass Transfer, 55 (2019) 2165–2171.
[52] A.S. Franca, L.S. Oliveira, M.E. Ferreira, Kinetics and equilibrium studies of methylene blue adsorption by spent coffee grounds, Desalination, 249 (2009) 267–272.
[53] A.F. Hassan, A.M. Abdel-Mohsen, M.M.G. Fouda, Comparative study of calcium alginate, activated carbon, and their composite beads on methylene blue adsorption, Carbohydr. Polym., 102 (2014) 192–198.
[54] J. Wu, D.J. Ren, X.Q. Zhang, Z.H. Chen, S.Q. Zhang, S. Li, L.J. Fu, The adsorption properties of biochar derived from woody plants or bamboo for cadmium in aqueous solution, Desal. Water Treat., 160 (2019) 268–275.
[55] M. El Ouardi, M. Laabd, H. Abou Oualid, Y. Brahmi, A. Abaamrane, A. Elouahli, A.A. Addi, A. Laknifli, Efficient removal of *p*-nitrophenol from water using montmorillonite clay: insights into the adsorption mechanism, process optimization, and regeneration, Environ. Sci. Pollut. Res., 26 (2019) 19615–19631.
[56] J.F. Lyu, H.X. Liu, Z.L.Z. Zeng, J.S. Zhang, Z.X. Xiao, P. Bai, X.H. Guo, Metal–organic framework UiO-66 as an efficient adsorbent for boron removal from aqueous solution, Ind. Eng. Chem. Res., 56 (2017) 2565–2572.
[57] C. Wang, Y.Y. Yang, J. Hou, P.F. Wang, L.Z. Miao, X. Wang, L.D. Guo, Optimization of cyanobacterial harvesting and extracellular organic matter removal utilizing magnetic nanoparticles and response surface methodology: a comparative study, Algal. Res., 45 (2020) 101756.
[58] R.R. Karri, J.N. Sahu, Process optimization and adsorption modeling using activated carbon derived from palm oil kernel shell for Zn(II) disposal from the aqueous environment using differential evolution embedded neural network, J. Mol. Liq., 265 (2018) 592–602.
[59] B.Y.Z. Hiew, L.Y. Lee, K.C. Lai, S.Y. Gan, S. Thangalazhy-Gopakumar, G.-T. Pan, T.C.-K. Yang, Adsorptive decontamination of diclofenac by three-dimensional graphene-based adsorbent: response surface methodology, adsorption equilibrium, kinetic and thermodynamic studies, Environ. Res., 168 (2019) 241–253.
[60] J. Kluczka, M. Gnus, A. Kazek-Kesik, G. Dudek, Zirconium-chitosan hydrogel beads for removal of boron from aqueous solutions, Polymer, 150 (2018) 109–118.
[61] J. Kluczka, W. Pudlo, K. Krukiewicz, Boron adsorption removal by commercial and modified activated carbons, Chem. Eng. Res. Des., 147 (2019) 30–42.
[62] L. Sun, J. Huang, H. Liu, Y. Zhang, X. Ye, H. Zhang, A. Wu, Z. Wu, Adsorption of boron by CA@KH-550@EPH@NMDG (CKEN) with biomass carbonaceous aerogels as substrate, J. Hazard. Mater., 358 (2018) 10–19.
[63] Z. Shu, Q. Guo, Y. Chen, J. Zhou, W. Guo, Y. Cao, Accelerated sorption of boron from aqueous solution by few-layer hydrotalcite nanosheets, Appl. Clay Sci., 149 (2017) 13–19.
[64] B. Wang, H. Lin, X. Guo, P. Bai, Boron removal using chelating resins with pyrocatechol functional groups, Desalination, 347 (2014) 138–143.
[65] I. Kipcak, M. Ozdemir, Removal of boron from aqueous solution using calcined magnesite tailing, Chem. Eng. J., 189 (2012) 68–74.